Capilla Romá, MT.; Talavera Usano, CF.; Ginestar Peiro, D.; Verdú Martín, GJ. (2017). A study of the radiative transfer equation using a spherical harmonics-nodal collocation method. Journal of Quantitative Spectroscopy and Radiative Transfer. 189:25-36. doi:10.1016/j.jqsrt.2016.11.008

A study of the radiative transfer equation using a spherical harmonics-nodal collocation method

M. T. Capilla[a], C. F. Talavera[a], D. Ginestar[a], G. Verdú[b,*]

[a] *Departamento de Matemática Aplicada, Universitat Politècnica de València, Camino de Vera 14, E-46022 Valencia, Spain*
[b] *Departamento de Ingeniería Química y Nuclear, Universitat Politècnica de València, Camino de Vera 14, E-46022 Valencia, Spain*

Abstract

Optical tomography has found many medical applications that need to know how the photons interact with the different tissues. The majority of the photon transport simulations are done using the diffusion approximation, but this approximation has a limited validity when optical properties of the different tissues present large gradients, when structures near the photons source are studied or when anisotropic scattering has to be taken into account. As an alternative to the diffusion model, the P_L equations for the radiative transfer problem are studied. These equations are discretized in a rectangular mesh using a nodal collocation method. The performance of this model is studied by solving different 1D and 2D benchmark problems of light propagation in tissue having media with isotropic and anisotropic scattering.

Keywords: radiative transfer equation, light propagation in tissue, multidimensional P_L equations, spherical harmonics, nodal collocation method
PACS: 02.60.Lj, 05.60.Cd, 87.57.-s, 87.90.+y

1. Introduction

Optical tomography, also referred to as diffuse optical tomography, has made considerable advances in recent years [1, 2]. This field is concerned with the use of visible and near-infrared light for diagnosis and treatment of biological tissues. Examples include optical monitoring of blood oxygenation, detection of cerebral hemorrhages, functional imaging of brain activity, diagnosis of Alzheimer's disease, breast cancer, etc. [3].

The use of optical techniques for medical imaging is an attractive alternative to other methods using ionizing radiation [4]. Optical imaging of the breast has undergone an important growth [5] as an imaging technique for the detection and

*Corresponding author.
Email addresses: tcapilla@mat.upv.es (M. T. Capilla), talavera@mat.upv.es (C. F. Talavera), dginesta@mat.upv.es (D. Ginestar), gverdu@iqn.upv.es (G. Verdú)

diagnosis of cancer. Optical techniques have also been applied to the detection and diagnosis of brain cancer, Alzheimer and other pathologies [6, 7, 8, 9]. These methods are different from other imaging techniques based on ionizing radiation because the light at the intensities used for diagnostic is not carcinogenic. A further motivation for using optical techniques based on photons is that these are sensitive to information related to metabolic processes and blood flow [3, 8], identifying different types of soft tissues. However, optical photons created in the near-infrared light spectrum suffer from scattering by heterogeneous bodies giving significant amount of blurring.

Having an efficient model to describe photon transport in tissue is fundamental in the medical application of optical radiation. Modeling of light propagation in tissue is largely done through the use of the diffusion approximation to the radiative transfer equation. But the diffusion approximation is only valid in optically thick media (the system must be large compared to the photon mean free path), far from any boundary layer, and when the absorption coefficient is small compared to the scattering coefficient. Since most biological tissues obey this condition, the diffusion approximation is often a good approximation and is frequently solved using finite elements techniques [10]. However, this model is not applicable to non-scattering void-like layers where the scattering and absorption are very low [11], and to regions where optical properties change a lot from the surrounding region [12]. Also, structures near to boundary source [13], clear regions, and anisotropic scattering cannot be fully taken into account with the diffusion approximation [14].

Providing solutions to the radiative transfer equation (RTE) remains a challenging task in the fields of tissue optics and radiological sciences. Limits of diffusion approximation have been investigated and compared with other methods by several researchers. Thus, in [9] the authors use a time-independent, discrete ordinates (S_N), finite difference transport code called DANTSYS that was developed by Alcouffe and co-workers and present the comparison of finite-difference transport and diffusion calculations for photon migration in homogeneous and heterogeneous tissues. To overcome known problems of the discrete ordinates method as the ray effect, the angular discretization of the RTE can be performed using spherical harmonics series. If the series is truncated at the Lth moment, the P_L approximation is obtained [12]. To try to overcome the complexity of the full P_L theory, an approximation based on simplified spherical harmonics, SP_L, has been successfully applied to 2D electron-photon problems [15], and to tissue optics [16]. Although the SP_L equations are fewer equations to solve than the full P_L equations, the SP_L solutions do not converge to exact transport solutions. On the other hand, the diffusive spherical harmonics P_L equations have several advantages regarding the S_N or SP_L equations. First, the diffusive P_L equations approximates the RTE equations by a set of coupled diffusion-like equations, which can be solved with standard diffusion solvers. Also, they do not suffer from ray effects, as the S_N method does. Yet, P_L equations can lead to highly oscillatory behavior and even negative particle concentrations [17, 18]. In the work of [6, 19] the authors developed a finite element spherical harmonics radiation transport model that is applied to this type of problems. All these

issues strongly suggest that the diffusive P_L spherical-harmonics equations can be applied to optical tomography, hence our interest in revisiting this field of medical imaging research.

In this paper, a spherical harmonics-nodal collocation method for the solution of the diffusive (second order) P_L equations is proposed. The angular P_L approximation is computed for arbitrary odd L. The spatial discretization is based on a nodal collocation method and the use of Legendre polynomials series on a coarse spatial mesh. The method has a rapid convergence with the number of Legendre polynomials, and the size of the discretized problem is smaller than the one obtained with other techniques as the finite difference method, when the same accuracy is required.

The present work is organized as follows: In Section 2, we introduce the radiative transfer equation for light propagation in tissue, and we review the multi-dimensional spherical harmonics P_L equations for arbitrary angular order L, that will be formulated as a vector-valued diffusive second order differential equation. Surface source and vacuum boundary conditions are approximated using Marshak's conditions and will be computed for arbitrary order L. The spatial discretization is then carried out using a nodal collocation method. In Section 3, several photon propagation problems are analyzed and used to validate the numerical accuracy of the P_L method described in Section 2. We examine the transport of photons through 1D and 2D homogeneous media, and also through 2D heterogeneous media with void-like regions and channels. In both types of media, cases with isotropic and anisotropic scattering are studied, considering in the last cases the Henyey-Greenstein and simplified approximated Mie phase functions. Finally the main conclusions of the study are summarized in Section 4.

2. The radiative transfer equation

The propagation of light in scattering media can be described by the radiative transfer equation (RTE), that is, the linearized one-speed, steady-state form of the Boltzmann transport equation [20]:

$$\vec{\Omega}\,\vec{\nabla}\Phi(\vec{r},\vec{\Omega}) + \mu_t(\vec{r})\,\Phi(\vec{r},\vec{\Omega}) = \int d\vec{\Omega}'\,\mu_s(\vec{r};\vec{\Omega}'\to\vec{\Omega})\,\Phi(\vec{r},\vec{\Omega}') + S(\vec{r},\vec{\Omega})\,, \qquad (1)$$

where $\Phi(\vec{r},\vec{\Omega})$ is the photon angular flux at the spatial point $\vec{r}=(x_1,x_2,x_3)$ and unit direction-of-flight $\vec{\Omega}=(\cos\varphi\,\sin\theta\,,\,\sin\varphi\,\sin\theta\,,\,\cos\theta)$, $0<\varphi<2\pi$, $0<\theta<\pi$; μ_t is the total macroscopic cross-section (attenuation coefficient), μ_s is the scattering cross-section from direction $\vec{\Omega}'$ to direction $\vec{\Omega}$ and finally $S(\vec{r},\vec{\Omega})$ is the internal fixed source term.

In the spherical harmonics method the angular dependence of the photon flux $\Phi(\vec{r},\vec{\Omega})$ and the source term $S(\vec{r},\vec{\Omega})$ are expanded in terms of the (complex) spherical harmonics $Y_l^m(\vec{\Omega}) = \sqrt{\frac{(2l+1)}{4\pi}\frac{(l-m)!}{(l+m)!}}\,P_l^m(\cos\theta)e^{im\varphi}$ [21] (where $P_l^m(\cos\theta)$ are the associated Legendre polynomials), that form a complete set

of orthonormal functions, that is, they satisfy the orthonormality property $\int d\vec{\Omega}\, {Y_m^l}^* Y_{m'}^{l'} = \delta_{ll'}\delta_{mm'}$, where δ_{ij} is the Kronecker delta and $d\vec{\Omega} = \sin\theta\, d\varphi d\theta$, $0 < \varphi < 2\pi$, $0 < \theta < \pi$. Thus,

$$\begin{aligned} \Phi(\vec{r},\vec{\Omega}) &= \sum_{l=0}^{\infty}\sum_{m=-l}^{+l} \phi_{lm}(\vec{r})\, Y_l^m(\vec{\Omega})\,, \\ S(\vec{r},\vec{\Omega}) &= \sum_{l=0}^{\infty}\sum_{m=-l}^{+l} s_{lm}(\vec{r})\, Y_l^m(\vec{\Omega})\,, \end{aligned} \tag{2}$$

where $\phi_{lm}(\vec{r})$ and $s_{lm}(\vec{r})$ are the (spherical harmonics) moments. Complex spherical harmonics will provide a more concise theoretical description of the method. The isotropic photon flux is then $\phi(\vec{r}) = \frac{1}{4\pi}\int d\vec{\Omega}\, \Phi(\vec{r},\vec{\Omega}) = (4\pi)^{-1/2}\phi_{00}(\vec{r})$.

It will also be assumed that scattering depends only on the relative angle between the incident and the scattered photons, $\vec{\Omega}\,\vec{\Omega}'$, and that the scattering cross-section may be expanded as the following series of Legendre polynomials

$$\mu_s(\vec{r},\vec{\Omega}\,\vec{\Omega}') = \sum_{l=0}^{\infty} \frac{2l+1}{4\pi}\mu_{s,l}(\vec{r})\, P_l(\vec{\Omega}\,\vec{\Omega}')\ . \tag{3}$$

In the process of light scattering in tissues the scattering cross-section is factorized as [22]

$$\mu_s(\vec{r},\vec{\Omega}\,\vec{\Omega}') = \mu_s(\vec{r})\, p(\vec{\Omega}\,\vec{\Omega}')\,,$$

where the *phase function* p is given by theoretical models and provides a convenient description of anisotropic scattering in terms of a unique parameter, the *anisotropy factor* g. Due to its simplicity, the most widely adopted is the Henyey-Greenstein (H-G) function [23]:

$$p_{\mathrm{HG}}(\vec{\Omega}\,\vec{\Omega}') = \frac{1-g^2}{4\pi(1+g^2-2g\vec{\Omega}\,\vec{\Omega}')^{3/2}} = \sum_{l=0}^{\infty}\frac{2l+1}{4\pi} g^l\, P_l(\vec{\Omega}\,\vec{\Omega}') \tag{4}$$

($g = 0$ corresponds to isotropic scattering). From (3) it is straightforward that the expansion coefficients are

$$\mu_{s,l}^{\mathrm{HG}}(\vec{r}) = \mu_s(\vec{r})\, g^l\,, \quad l = 0, 1, \ldots$$

This model is inefficient in the forward peaked range ($g > 0.8$) due to the high number of Legendre expansion coefficients required [6]. So recently a new scattering phase function, the simplified approximate Mie (SAM), has been proposed [24] that requires less coefficients:

$$p_{\mathrm{SAM}}(\vec{\Omega}\,\vec{\Omega}') = K_S(1+\vec{\Omega}\,\vec{\Omega}')^{n_p}\,, \tag{5}$$

where $n_p = \frac{2g}{1-g}$ is the anisotropic index and $K_S = \frac{1}{2\pi}\frac{n_p+1}{2^{n_p+1}}$ is the normalization factor. Now, the expansion coefficients in (3) are given by

$$\mu_{s,l}^{\mathrm{SAM}}(\vec{r}) = \mu_s(\vec{r})\frac{n_p+1}{2^{n_p+1}}\int_{-1}^{1}(1+\omega)^{n_p} P_l(\omega)\, d\omega\,, \quad l = 0, 1, \ldots$$

Expansions (2) and (3) and the orthogonality properties of Y_l^m are then used into (1). Let us consider the first term in (1), that accounts for photons removed by leakage in direction $\vec{\Omega}$. If $\vec{\Omega}\,\vec{\nabla}\Phi(\vec{r},\vec{\Omega}) = \sum_{l'=0}^{\infty}\sum_{m'=-l'}^{+l'} A_{l'm'}(\vec{r})Y_{l'}^{m'}(\vec{\Omega})$ then (for simplicity, we omit the arguments of Y_l^m and Φ)

$$
\begin{aligned}
A_{l'm'} &= \int d\vec{\Omega}\, Y_{l'}^{m'\,*}(\vec{\Omega}\,\vec{\nabla}\Phi) \\
&= \sum_{\substack{l=0 \\ -l\le m\le +l}}^{\infty} \Big[\int d\vec{\Omega}\, Y_{l'}^{m'\,*}\cos\varphi\sin\theta\, Y_l^m\,\frac{\partial\phi_{lm}}{\partial x_1} + \int d\vec{\Omega}\, Y_{l'}^{m'\,*}\sin\varphi\sin\theta\, Y_l^m\,\frac{\partial\phi_{lm}}{\partial x_2} \\
&\qquad\qquad + \int d\vec{\Omega}\, Y_{l'}^{m'\,*}\cos\theta\, Y_l^m\,\frac{\partial\phi_{lm}}{\partial x_3}\Big]\,.
\end{aligned}
$$

If we have into account the following formulas

$$
\begin{aligned}
\int d\vec{\Omega}\, Y_{l'}^{m'\,*}\sin\theta\, e^{-i\varphi}\, Y_l^m &= \big(-C_1(l,m)\delta_{l-1,l'} + C_2(l',m')\delta_{l'-1,l}\big)\delta_{m'+1,m}\,, \\
\int d\vec{\Omega}\, Y_{l'}^{m'\,*}\sin\theta\, e^{i\varphi}\, Y_l^m &= \big(-C_1(l',m')\delta_{l'-1,l} + C_2(l,m)\delta_{l-1,l'}\big)\delta_{m+1,m'}\,, \\
\int d\vec{\Omega}\, Y_{l'}^{m'\,*}\cos\theta\, Y_l^m &= \big(C_3(l,m)\delta_{l-1,l'} + C_3(l',m')\delta_{l'-1,l}\big)\delta_{m',m}\,,
\end{aligned}
$$

where

$$
\begin{aligned}
C_1(l,m) &= \left(\frac{(l+m)(l+m-1)}{(2l+1)(2l-1)}\right)^{1/2}\,, \\
C_2(l,m) &= C_1(l,-m)\,, \\
C_3(l,m) &= \left(\frac{(l+m)(l-m)}{(2l+1)(2l-1)}\right)^{1/2}\,,
\end{aligned}
$$

it follows that

$$
\begin{aligned}
A_{l'm'} = \sum_{\substack{l=0 \\ -l\le m\le +l}}^{\infty} \Bigg\{ & \frac{1}{2}\Big[\big(-C_1(l,m)\delta_{l-1,l'} + C_2(l',m')\delta_{l'-1,l}\big)\delta_{m'+1,m} \\
& + \big(-C_1(l',m')\delta_{l'-1,l} + C_2(l,m)\delta_{l-1,l'}\big)\delta_{m+1,m'}\Big]\frac{\partial\phi_{lm}}{\partial x_1} \\
& + \frac{1}{2i}\Big[\big(-C_1(l,m)\delta_{l-1,l'} + C_2(l',m')\delta_{l'-1,l}\big)\delta_{m'+1,m} \\
& + \big(-C_1(l',m')\delta_{l'-1,l} + C_2(l,m)\delta_{l-1,l'}\big)\delta_{m+1,m'}\Big]\frac{\partial\phi_{lm}}{\partial x_2} \\
& + \big(C_3(l,m)\delta_{l-1,l'} + C_3(l',m')\delta_{l'-1,l}\big)\delta_{m',m}\frac{\partial\phi_{lm}}{\partial x_3}\Bigg\}\,. \qquad (6)
\end{aligned}
$$

Let us now consider the scattering source term in the equation (1). Knowing that the Legendre polynomials of a scalar product of unit vectors can be expanded as $P_l(\vec{\Omega}\,\vec{\Omega}') = \frac{4\pi}{2l+1}\sum_{m=-l}^{l} Y_l^m(\vec{\Omega})Y_l^{m*}(\vec{\Omega}')$, and using the assumption

(3), we get

$$\int d\vec{\Omega}' \sum_{l=0}^{\infty} \frac{2l+1}{4\pi} \mu_{s,l}(\vec{r}) P_l(\vec{\Omega}\,\vec{\Omega}') \Phi(\vec{r},\vec{\Omega}')$$
$$= \int d\vec{\Omega}' \sum_{l=0}^{\infty} \sum_{m=-l}^{l} \mu_{s,l}(\vec{r}) Y_l^m(\vec{\Omega}) Y_l^{m*}(\vec{\Omega}') \Phi(\vec{r},\vec{\Omega}') = \sum_{\substack{l=0 \\ -l\le m\le +l}}^{\infty} \mu_{s,l}\, Y_l^m(\vec{\Omega}) \phi_{lm}(\vec{r})\,.$$

From these expressions it is straightforward to obtain the following (infinite) set of (complex) equations for the spherical harmonics moments ϕ_{lm}:

$$\begin{aligned}
&\frac{1}{2}\Big(-C_1(l+1,m+1)\frac{\partial \phi_{l+1,m+1}}{\partial x_1} + C_2(l,m)\frac{\partial \phi_{l-1,m+1}}{\partial x_1} \\
&\qquad - C_1(l,m)\frac{\partial \phi_{l-1,m-1}}{\partial x_1} + C_2(l+1,m-1)\frac{\partial \phi_{l+1,m-1}}{\partial x_1}\Big) \\
&+ \frac{1}{2i}\Big(-C_1(l+1,m+1)\frac{\partial \phi_{l+1,m+1}}{\partial x_2} + C_2(l,m)\frac{\partial \phi_{l-1,m+1}}{\partial x_2} \\
&\qquad - C_1(l,m)\frac{\partial \phi_{l-1,m-1}}{\partial x_2} + C_2(l+1,m-1)\frac{\partial \phi_{l+1,m-1}}{\partial x_2}\Big) \\
&+ C_3(l+1,m)\frac{\partial \phi_{l+1,m}}{\partial x_3} + C_3(l,m)\frac{\partial \phi_{l-1,m}}{\partial x_3} + \mu_t\,\phi_{lm} \\
&= \mu_{s,l}\,\phi_{lm} + s_{lm}\,, \qquad l = 0,1,\ldots, \quad m = -l,\ldots,+l\,.
\end{aligned} \tag{7}$$

It is understood that terms involving moments ϕ_{lm} with invalid indices l and m are zero. To obtain a finite approximation, the series in expansions (2) and (3) are truncated at some finite order $l = L$ and the resulting equations (7) are known as the P_L equations. In the following, we will only consider L to be an odd integer.

We observe that the radiative transfer equation (1) is a real equation and, as we are interested (for physical reasons) on real solutions, then $\Phi = \Phi^*$, that is, ${\phi_{lm}}^* = (-1)^m \phi_{l,-m}$ and not all complex moments are independent so there are only $2l+1$ real independent moments for each $l > 0$, that is, $\{\phi_{l0}, \mathrm{Re}\,\phi_{lm}, \mathrm{Im}\,\phi_{lm}, m = 1,\ldots,l\}$. We will now obtain the real form of P_L equations (7). Taking real and imaginary part in (7) and defining the real moments

$$\begin{aligned}
\xi_{lm} &= \mathrm{Re}\,\phi_{lm} = \frac{1}{2}(\phi_{lm} + (-1)^m \phi_{l,-m})\,, \\
\eta_{lm} &= \mathrm{Im}\,\phi_{lm} = \frac{1}{2i}(\phi_{lm} - (-1)^m \phi_{l,-m})\,,
\end{aligned} \tag{8}$$

we obtain the corresponding $2l+1$ real equations:

$$\begin{aligned}
&\frac{1}{2}\Big(-C_1(l+1,m+1)\frac{\partial \xi_{l+1,m+1}}{\partial x_1} + C_2(l,m)\frac{\partial \xi_{l-1,m+1}}{\partial x_1} \\
&\qquad - C_1(l,m)\frac{\partial \xi_{l-1,m-1}}{\partial x_1} + C_2(l+1,m-1)\frac{\partial \xi_{l+1,m-1}}{\partial x_1}\Big) \\
&+ \frac{1}{2}\Big(-C_1(l+1,m+1)\frac{\partial \eta_{l+1,m+1}}{\partial x_2} + C_2(l,m)\frac{\partial \eta_{l-1,m+1}}{\partial x_2} \\
&\qquad - C_1(l,m)\frac{\partial \eta_{l-1,m-1}}{\partial x_2} + C_2(l+1,m-1)\frac{\partial \eta_{l+1,m-1}}{\partial x_2}\Big) \\
&+ C_3(l+1,m)\frac{\partial \xi_{l+1,m}}{\partial x_3} + C_3(l,m)\frac{\partial \xi_{l-1,m}}{\partial x_3} + \mu_t\,\xi_{lm} \\
&\quad = \mu_{s,l}\,\xi_{lm} + \operatorname{Re} s_{lm}\,, \qquad m = 0,1,\ldots,l\,,
\end{aligned} \tag{9}$$

and

$$\begin{aligned}
&\frac{1}{2}\Big(-C_1(l+1,m+1)\frac{\partial \eta_{l+1,m+1}}{\partial x_1} + C_2(l,m)\frac{\partial \eta_{l-1,m+1}}{\partial x_1} \\
&\qquad - C_1(l,m)\frac{\partial \eta_{l-1,m-1}}{\partial x_1} + C_2(l+1,m-1)\frac{\partial \eta_{l+1,m-1}}{\partial x_1}\Big) \\
&- \frac{1}{2}\Big(-C_1(l+1,m+1)\frac{\partial \xi_{l+1,m+1}}{\partial x_2} + C_2(l,m)\frac{\partial \xi_{l-1,m+1}}{\partial x_2} \\
&\qquad - C_1(l,m)\frac{\partial \xi_{l-1,m-1}}{\partial x_2} + C_2(l+1,m-1)\frac{\partial \xi_{l+1,m-1}}{\partial x_2}\Big) \\
&+ C_3(l+1,m)\frac{\partial \eta_{l+1,m}}{\partial x_3} + C_3(l,m)\frac{\partial \eta_{l-1,m}}{\partial x_3} + \mu_t\,\eta_{lm} \\
&\quad = \mu_{s,l}\,\eta_{lm} + \operatorname{Im} s_{lm}\,, \qquad m = 1,\ldots,l\,,
\end{aligned} \tag{10}$$

From the index structure of the equations (9) and (10), it is convenient to gather even l moments into vectors

$$X = (\xi_{l,m\geq 0}, \eta_{l,m>0})_{l=\text{even}}\,, \qquad \mathcal{S} = (\operatorname{Re} s_{l,m\geq 0}, \operatorname{Im} s_{l,m>0})_{l=\text{even}}\,, \tag{11}$$

with $n_e = L(L+1)/2$ components, and odd l moments into vectors

$$\bar{X} = (\xi_{l,m\geq 0}, \eta_{l,m>0})_{l=\text{odd}}\,, \qquad \bar{\mathcal{S}} = (\operatorname{Re} s_{l,m\geq 0}, \operatorname{Im} s_{l,m>0})_{l=\text{odd}}\,, \tag{12}$$

with $n_o = (L+1)(L+2)/2$ components (for example, if $L=1$ then $X = (\xi_{00})$ and $\bar{X} = (\xi_{10}, \xi_{11}, \eta_{11})^T$). Then (9) and (10) can be rewritten as

$$\sum_{j=1}^{3} M_j \frac{\partial \bar{X}}{\partial x_j} + \operatorname{diag}(\mu_t - \mu_{sl})_{l=\text{even}} X = \mathcal{S}\,, \tag{13}$$

$$\sum_{j=1}^{3} \bar{M}_j \frac{\partial X}{\partial x_j} + \operatorname{diag}(\mu_t - \mu_{sl})_{l=\text{odd}} \bar{X} = \bar{\mathcal{S}}\,, \tag{14}$$

where M_j and $\bar{M}_j$ are rectangular matrices of dimensions $n_e \times n_o$ and $n_o \times n_e$ respectively, defined from the coefficients of (9) and (10). Eq. (14) relates $\bar{X}$ with derivatives of X so it corresponds to a generalization of "Fick's law":

$$\bar{X} = -D \sum_{j=1}^{3} \bar{M}_j \frac{\partial X}{\partial x_j} + D\,\bar{\mathcal{S}}\,, \tag{15}$$

where $D = \mathrm{diag}(\mu_t - \mu_{sl})^{-1}_{l=\mathrm{odd}}$ is a square matrix. Replacing (15) into (13) we obtain the "diffusive form of P_L equations":

$$-\sum_{i,j=1}^{3} \frac{\partial}{\partial x_i}\Big(M_i D \bar{M}_j \frac{\partial X}{\partial x_j}\Big) + \mu_a X = \mathcal{S}_{\mathrm{eff}}\,, \tag{16}$$

where $\mu_a = \mathrm{diag}(\mu_t - \mu_{sl})_{l=\mathrm{even}}$ is the absorption coefficient and the "effective source term" is $\mathcal{S}_{\mathrm{eff}} = \mathcal{S} - \sum_{j=1}^{3} \frac{\partial}{\partial x_j}(M_j D \bar{\mathcal{S}})$. The square "effective diffusion matrices" $M_i D \bar{M}_j$ generalize the diffusion coefficient $1/(3(\mu_t - \mu_{s1}))$ of P_1 equation to P_L equations for $L > 1$. Notice that the equation (16) will encounter difficulties when dealing with problems that involve void regions, where matrix D is (near) singular.

Finally, (16) corresponds to 3D geometry. Lower dimensional geometries are obtained by imposing restrictions to the angular flux. The XY (2D) geometry is obtained considering that the angular flux does not depend on the third coordinate, $\Phi = \Phi(x_1, x_2, \vec{\Omega})$, so $\frac{\partial \Phi}{\partial x_3} = 0$, and also must satisfy the symmetry relation $\Phi(\theta) = \Phi(\pi - \theta)$, so the moments $\phi_{lm} = 0$ if $l + m$ is odd. The planar (1D) geometry is obtained by imposing that the photon flux $\Phi = \Phi(x_3, \theta)$ so the only non-zero moments are $\phi_{l,m=0} = \xi_{l0}$ and they are also real.

2.1. Boundary conditions

When an external surface source is located at the boundary of the region described by (1), the angular photon flux is specified by $T(r, \vec{\Omega})$ for every incoming direction,

$$\Phi(\vec{r}, \vec{\Omega}) = T(r, \vec{\Omega})\ , \qquad \text{for all } \ \vec{\Omega}\,\vec{n} \leq 0\ , \tag{17}$$

where $\vec{n}$ is the outwardly directed unitary normal vector to the external surface. Vacuum boundary conditions, in particular, correspond to $T = 0$. This condition can be approximated by setting Marshak's conditions [25]

$$\int_{\vec{\Omega}\,\vec{n}\leq 0} d\vec{\Omega}\ Y_l^{m*}(\vec{\Omega})\,\big(\Phi(\vec{r}, \vec{\Omega}) - T(\vec{r}, \vec{\Omega})\big) = 0\ , \tag{18}$$

for $l = 1, 3, 5, \ldots, L\,(\mathrm{odd})$ and $m = 0, 1, \ldots, l$ (the conditions with negative m index are redundant because the photon flux Φ is a real function). Notice that (18) is complex so there are $2l + 1$ real conditions for each odd index l.

We will only consider regions with prismatic geometry; we can then use the symmetry $Y_l^m(-\vec{\Omega}) = (-1)^l Y_l^m(\vec{\Omega})$ obtaining that, for $l + l'$ even,

$$\int_{\vec{\Omega}\,\vec{n}\leq 0} d\vec{\Omega}\ Y_l^{m*}(\vec{\Omega})\,Y_{l'}^{m'}(\vec{\Omega}) = \frac{1}{2}\int_{\vec{\Omega}} d\vec{\Omega}\ Y_l^{m*}(\vec{\Omega})\,Y_{l'}^{m'}(\vec{\Omega}) = \frac{1}{2}\delta_{ll'}\,\delta_{mm'}\,. \tag{19}$$

Inserting the expansion given by the equation (2) for Φ and also for the external source,

$$T(\vec{r},\vec{\Omega}) = \sum_{l=0}^{\infty} \sum_{m=-l}^{+l} T_{lm}(\vec{r}) Y_l^m(\vec{\Omega}) \,,$$

truncated up to a finite odd order L, into Marshak's conditions (18) and using (19), it results into the conditions

$$\frac{1}{2}(\phi_{lm} - T_{lm}) + \sum_{\substack{l' \text{ even} \\ -l' \le m' \le l'}}^{L-1} \Big(\int_{\vec{\Omega}\,\vec{n} \le 0} d\vec{\Omega}\; Y_l^{m*}(\vec{\Omega})\, Y_{l'}^{m'}(\vec{\Omega}) \Big) (\phi_{l'm'} - F_{l'm'}) = 0 \,, \quad (20)$$

for $l = 1, 3, 5, \ldots, L$ and $m = 0, 1, \ldots, l$. Taking real and imaginary part in (20), Marshak's conditions can be written as

$$(\bar{X} - \bar{T}) + N^V (X - T) = 0 \;, \quad (21)$$

that is,

$$\bar{X} + N^V X = \bar{T} + N^V T \,, \quad (22)$$

where real vectors X and $\bar{X}$ were defined in (11) and (12), also

$$T = (\mathrm{Re}\, T_{l,m\ge 0}, \mathrm{Im}\, T_{l,m>0})_{l=\text{even}} \,, \quad \bar{T} = (\mathrm{Re}\, T_{l,m\ge 0}, \mathrm{Im}\, T_{l,m>0})_{l=\text{odd}} \,,$$

and N^V is a real rectangular matrix (of dimensions $n_o \times n_e$) whose numerical values depend on the geometry of the boundary surface, that is, the spatial axis normal to the boundary surface.

2.2. The nodal collocation method for an isotropic source

Since P_L equations (16) have a diffusive form, their spatial discretization can be done using a nodal collocation method, previously used for the neutron diffusion equation [26, 27] and generalized for eigenvalue problems in multidimensional rectangular geometries [28, 29]. For simplicity, in this work we will only apply the method when the internal source $S(\vec{r},\vec{\Omega})$ in (1) is isotropic. This implies that $\bar{\mathcal{S}} = 0$ and no source term appears in Fick's law (15). This situation was studied in [29] so we will only briefly describe the method for 3D geometry.

Given an structured rectilinear mesh with vertex coordinates $\{x_{1,i_1}, x_{2,i_2}, x_{3,i_3}\}$, where $i_j = 0, 1, \ldots, m_j$ $(j = 1, 2, 3)$ are vertex indices, we only consider a domain that can be divided into N $(\le m_1 m_2 m_3)$ adjacent rectangular prisms, or nodes, of the form $N^e = [x_{1,i_1}, x_{1,i_1+1}] \times [x_{2,i_2}, x_{2,i_2+1}] \times [x_{3,i_3}, x_{3,i_3+1}]$, being $e = 1, \ldots, N$ the index that enumerates the nodes, once an appropriate node ordering has been chosen, see Fig. 1.

For a generic node N^e the following change of variables

$$u_j = \frac{1}{\Delta x_j^e} \Big(x_j - \frac{1}{2}(x_{j,i_j} + x_{j,i_j+1}) \Big) \,, \quad j = 1, 2, 3 \,, \quad (23)$$

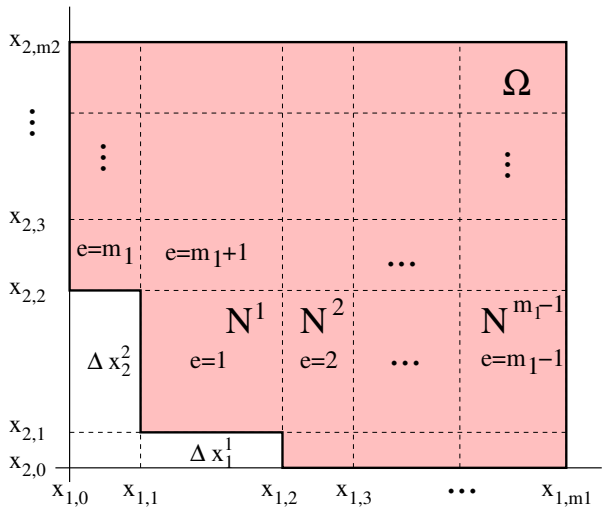

Figure 1: Sample rectilinear mesh covering the domain for 2D geometry. A *natural* ordering for spatial nodes N^e has been chosen.

where $\Delta x_j^e = x_{j,i_j+1} - x_{j,i_j}$, transforms the node N^e into the cubic node of volume one $N_u^e = [-\frac{1}{2}, +\frac{1}{2}]^3$.

The nodal collocation method assumes that on each node the cross-sections and the internal source term in (1) are constant. For each node N^e, the P_L equations (16) are transformed by means of the change of variables (23). Furthermore, if $X^e(u_1, u_2, u_3)$ denotes the previously defined vector of l even moments that appears in (16) for node N^e, it is assumed that spatial dependence of vector X^e can be expanded in terms of (orthonormal) Legendre polynomials $\mathcal{P}_k(u)$ [28] up to a certain finite order M,

$$X^e(u_1, u_2, u_3) = \sum_{k_1,k_2,k_3=0}^{M} x^e_{k_1 k_2 k_3} \mathcal{P}_{k_1}(u_1)\, \mathcal{P}_{k_2}(u_2)\, \mathcal{P}_{k_2}(u_3)\,, \tag{24}$$

where $u_j \in [-\frac{1}{2}, +\frac{1}{2}]$, $j = 1, 2, 3$, and the Legendre coefficients $x^e_{k_1 k_2 k_3}$ are the unknowns to be determined. Notice that polynomial expansion of the source term $\mathcal{S}^e_{\text{eff}}$ at node N^e reduces to the constant term. The series (24) is then inserted into (16) and equations for $x^e_{k_1 k_2 k_3}$ are derived using the orthonormality properties of $\mathcal{P}_k(u)$.

Double derivative terms in (16) will involve coupling with neighboring nodes. When node N^e is an interior node, adjacent nodes are related imposing continuity of the photon angular flux $\Phi(\vec{r}, \vec{\Omega})$ (or, equivalently, of all moments X^e and $\bar{X}^e$) at the interface between nodes. In the case that the node N^e is adjacent to a boundary, then Marshak's boundary conditions (22) are used. See [28, 29] for further details.

Finally, once an appropriate ordering of the indices is chosen, the previous procedure approximates the equations (16) by an algebraic problem that can be casted in the form

$$\mathcal{A}\,V = \mathcal{S}\,, \tag{25}$$

where V is a real vector of components $(\xi^e_{l,m\geq 0;k_1k_2k_3}, \eta^e_{l,m>0;k_1k_2k_3})$, $\mathcal{S}$ is the independent term associated with the source term and the external surface source and $\mathcal{A}$ is a matrix of dimension

$$N \times N_{\rm Leg} \times n_e = N \times M^d \times \frac{L(L+1)}{2}\,, \tag{26}$$

where N is the number of nodes; $N_{\rm Leg}$ is the number of Legendre moments, being M the order in Legendre series (24) and d the spatial dimension; and finally n_e is the number of components of vector X in (11), being L the order of the P_L approximation. Problem (25) is a system of linear equations that is large and sparse. The linear system is then iteratively solved using the bi-conjugate gradient stabilized method BICGSTAB, with an incomplete LU factorization, ILUT, as preconditioner, from the FORTRAN library SPARSKIT [30].

In previous works [28, 29] we investigated the convergence of the nodal collocation method, with different number of discretization nodes and different order M of Legendre polynomials used in the expansion (24). We observed that the convergence is largely improved increasing the degree of the polynomials considered (for $M = 1$, there is a slow spatial convergence). Also, we observed that, from the computational point of view, it is more favorable increasing the polynomial order M than increasing the number of discretization nodes [29].

3. Numerical results

In this Section, we present some numerical results in order to evaluate the performance and numerical accuracy of the nodal collocation method. The method has been already tested with neutron transport problems that are driven by internal sources [31] and also with eigenvalue problems [29]. The formulation described above has been implemented in the multi-group radiation transport code SHNC (Spherical Harmonics-Nodal Collocation), written in FORTRAN 90, which solves the external fixed source problem for an arbitrary P_L approximation for odd L, and we show its application as a light propagation model for biological homogeneous and heterogeneous tissues by choosing appropriate numerical examples.

We present results for a one-dimensional problem, comparing the numerical P_L results to the analytical solution. Also we present several two-dimensional cases where we compare the P_L photon fluxes to S_N results obtained from the code DANTSYS [32], taken as reference. In some cases our solutions are also compared to solutions from the literature. Computation times vary from several seconds to several minutes, depending on the size of the spatial mesh and the order of the P_L approximation, on a workstation with AMD Phenom II 1055T processor and 16Gb of memory, using only one processor for each computation.

Since the primary purpose of this work is to verify the capability of the SHNC code to solve the photon propagation problems with accuracy with respect to reference results, providing details of the numerical P_L approximations, the computational efficiency in solving the P_L equations was not the priority of this study.

3.1. One-dimensional homogeneous medium

To validate our code, we first analyze a test example consisting of a simple homogeneous one-dimensional region of finite length, where analytical solution exists.

We obtain the 1D transport equation for plane symmetry when the medium is transversely infinite (in the x_1x_2 plane) with cross sections and source variation only in the x_3 direction. For this case, the radiative transfer equation (1) becomes

$$\omega \frac{d\Phi}{dz}(z,\omega) + \mu_t\, \Phi(z,\omega) = 0\,, \quad 0 < z < l\,, \tag{27}$$

where we have defined $z = x_3$, $\omega = \cos\theta \in [-1,1]$, then the photon flux $\Phi = \Phi(z,\omega)$; the scattering and absorption coefficients considered for this region are $\mu_s = 0$ and $\mu_a \neq 0$, far away from a diffusive (P_1) regime. Finally, we set an external source T at $z = 0$ and vacuum boundary condition at the other side:

$$\begin{aligned} &\Phi(0,\omega) = T(0,\omega)\,, \quad \text{if } \ 0 < \omega \leq +1\,, \\ &\Phi(l,\omega) = 0\,, \qquad \text{if } \ -1 \leq \omega < 0\,. \end{aligned} \tag{28}$$

If $\omega \neq 0$ is kept fixed, the general solution of the first order ordinary differential equation (27) is $\Phi(z,\omega) = C(\omega)e^{-\frac{\mu_t}{\omega}z}$, where $C(\omega)$ is a function only of ω. If we impose the boundary conditions (28) we get

$$\Phi(z,\omega) = \begin{cases} T(0,\omega)\, e^{-\frac{\mu_t}{\omega}z} & \text{if } \ 0 < \omega \leq +1\,, \\ 0 & \text{if } \ -1 \leq \omega < 0\ . \end{cases} \tag{29}$$

Then the isotropic photon flux is

$$\phi(z) = \frac{1}{2}\int_{-1}^{+1} d\omega\, \Phi(z,\omega) = \frac{1}{2}\int_{0}^{+1} d\omega\, T(0,\omega)\, e^{-\frac{\mu_t}{\omega}z}\,. \tag{30}$$

For the numerical calculations a slab of length 10 mm is considered, with an isotropic external source $T(0,\omega) = 1$ photons/mm located at $z = 0$ mm and vacuum boundary condition applied at the right boundary, as shown in Fig. 2. The absorption coefficient considered is $\mu_a = 0.1$ mm^{-1}.

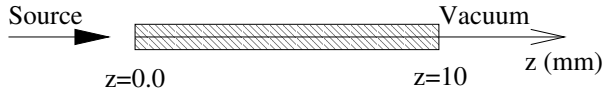

Figure 2: Geometry of the one-dimensional slab problem.

We have performed the numerical P_L solutions for the photon fluxes with the SHNC code. We have used for the calculations a mesh consisting of 10 nodes with size 1 mm and the order of the Legendre polynomials expansion considered in (24) is $M = 4$.

Fig. 3 shows the photon flux as function of the distance z from the external source, calculated with the P_L approximations for $L = 1, 3, 7, 9$, together with the analytical solution (29), obtained by numerical integration using Quadpack [33]. The figure also shows the S_{24} solution obtained with the discrete-ordinates code ONEDANT [32], with 1000 mesh points.

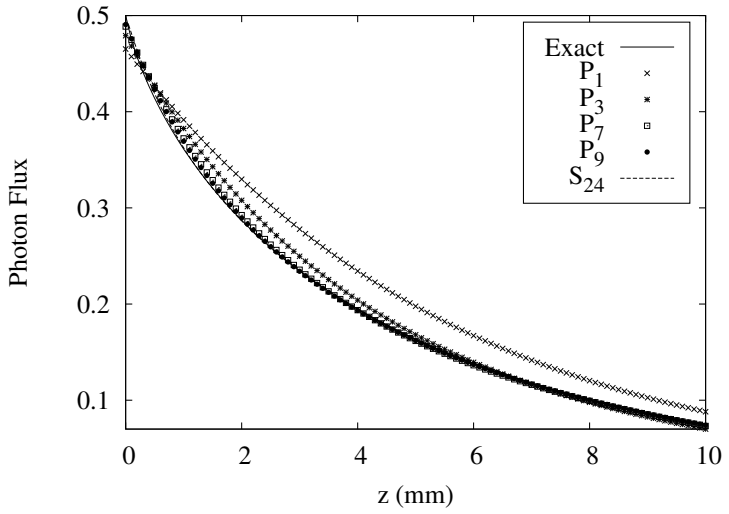

Figure 3: Photon fluxes for the homogeneous one-dimensional problem.

As can be seen from this figure, the P_1 approximation, as expected, fails to describe the light propagation correctly, whereas higher order P_L approximations (P_7, P_9) show accurate results in comparison to the exact solution.

3.2. Two-dimensional homogeneous media

A second example to study the application of the nodal collocation method in homogeneous media is a two-dimensional 10 mm $\times$10 mm square. The simulation geometry of this problem is shown in Fig. 4. From now on we will consider $x = x_1$ and $y = x_2$. A single isotropic light source with spatial size of 2 mm is symmetrically localized on the left boundary near $y = 5$ mm, at $x = 0$ mm, and 4 mm $< y <$ 6 mm. Vacuum boundary conditions are applied on all the other boundaries.

This small model with area of 100 mm^2 enables us to analyze the accuracy of the P_L solutions in problems with small tissue geometries, where boundary

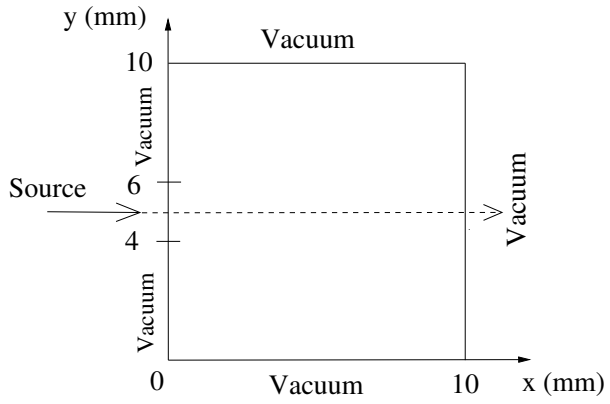

Figure 4: Geometry of the two-dimensional homogeneous medium.

effects would dominate the light propagation. These cases simulate the scattering and absorption physics of a 2D transverse tissue slice of small animals [16].

We consider three numerical examples with the same geometry (see Fig. 4) by varying the absorption coefficient, the scattering coefficient, and the anisotropy factor. In the first test, we will consider a model with $\mu_s = 0$, then we will expect large deviations between P_1 and P_L (for $L > 1$) solutions. Also, we will study the influence of the optical parameters on the accuracy of the P_L solutions in media with a difussive regime where $\mu_a \ll \mu_s'$, where a good match between all the P_L solutions is expected, and also we will analyze the impact of the anisotropic scattering in these types of media.

The P_L calculations were performed using a mesh consisting of 10×10 nodes with side length 1 mm and the order of the Legendre polynomials considered in (24) is $M = 4$. We observe that in all the problems, the convergence of the nodal collocation method is already achieved when a moderate number of polynomials is considered.

In each case, the P_L results are compared with the solution obtained with the S_N code TWODANT [32] taken as reference, with a 500×500 grid and a convergence criterion of 10^{-7}.

3.2.1. 2D homogeneous test case A

In this case the absorption coefficient considered is $\mu_a = 0.1$ mm^{-1} and there is no scattering. We present the P_L photon flux solutions for odd L and $1 \leq L \leq 9$. As $\mu_s = 0$, we anticipate discrepancies between P_1 and P_L ($L > 1$) solutions. We also calculate the S_N photon flux with TWODANT code and, in order to minimize the well known ray effect, we have set $N = 24$ (S_{24}) in the calculations. In low scattering regions or strong absorbers the discretization schemes based on the discrete ordinates solution often exhibit rays along the discrete directions when solving the RTE [34]. The solution is highly oscillatory,

and this effect is exacerbated by singular type sources, such as spatially localized sources. Ray effects can cause large errors in pointwise quantities such as the photon flux. The P_L approximation does not suffer from the ray effect.

In this test case the P_L results will be closer to the S_{24} transport solution as the order L increases, although one cannot draw conclusions about the accuracy of the P_L results in comparison with the S_{24} solution due to the presence of large ray effects in this latter.

The photon flux results are plotted in Fig. 5 along the horizontal line $y = 5$ mm passing through the source. The figure shows the P_L ($L = 1, \ldots, 9$) and S_{24} solutions.

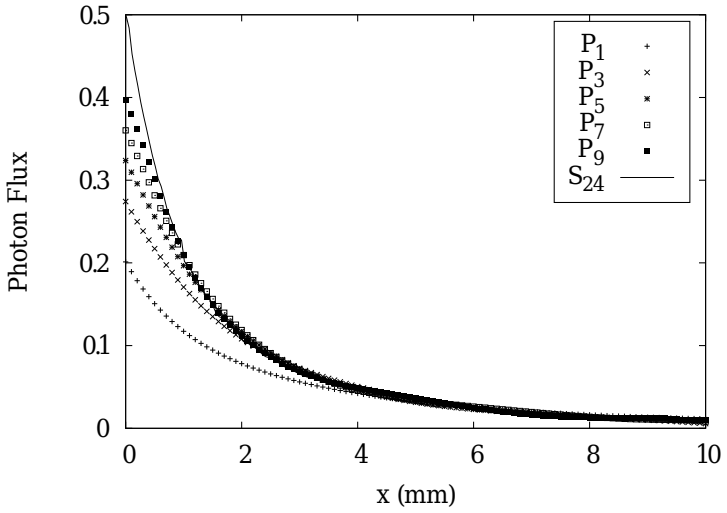

Figure 5: Photon fluxes for the homogeneous 2D case A along $y = 5$ mm.

As it was expected, large deviations between P_1 and P_L (for $L > 1$) can be observed in Fig. 5, and the P_L photon flux increases for large values of L. Along $y = 5$ mm, the P_9 flux does not reach the S_{24} solution. To illustrate the analysis of these results, the contour plots of the P_9 and S_{24} flux distributions are given in Fig. 6, where we can see clearly that the S_{24} contour map shows rays emanating from the source.

In the following sections, some tests will be treated to further analyze the accuracy of the P_L solutions.

3.2.2. 2D isotropic scattering test case B

This test case is based on a work presented in [16]. We consider an isotropically scattering tissue-like medium with $\mu_s = 1$ mm^{-1} and $\mu_a = 0.1$ mm^{-1} ($\Rightarrow \mu_t = 1.1$ mm^{-1}), then it holds that $\mu_a \ll \mu_s$ which means that good agreement between P_1, P_L ($L > 1$) and S_{24} solutions is expected.

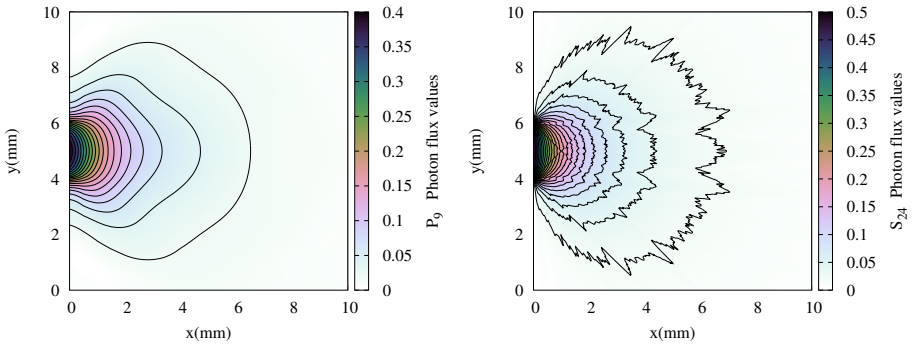

Figure 6: Contour map of the photon flux distribution, obtained with P_9 approximation (left) and S_{24} (right), for the homogeneous 2D case A.

Fig. 7 shows the photon fluxes along X-axis through medium center ($y = 5$ mm), modeled by P_L ($L = 1, 3, 7$) together with the S_{24} solution. The figure includes a detail of the zone for $0.8 < x < 1.2$ mm, where we observe that the S_{24} solution presents very slight oscillations due to the ray effect.

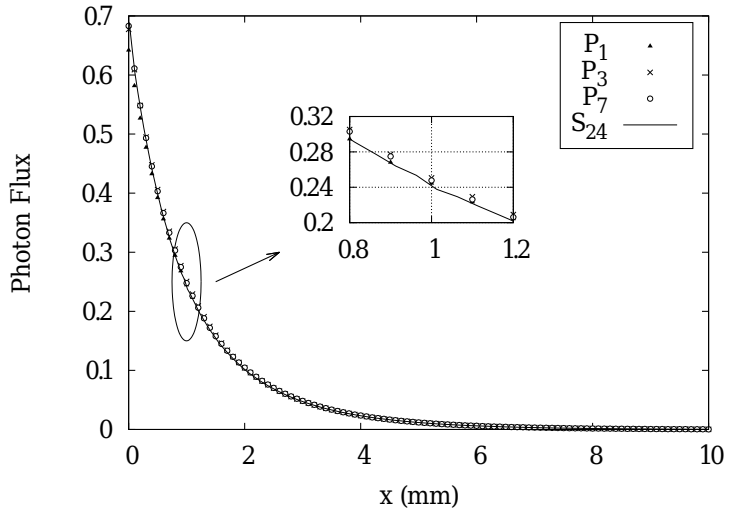

Figure 7: Photon fluxes for the homogeneous 2D case B along $y = 5$ mm.

In order to quantify the difference of each P_L photon flux with respect to the S_{24} solution, we use the model error of the flux inside the medium at an interior grid point x_i along the X-axis [16]. The model error σ^{ϕ}_{Mi} is given by the relative percentage difference at the point x_i of the flux ϕ_i of the P_L approximation with respect to the flux $\widetilde{\phi}_i$ of the S_{24} method. We also define the total model error

σ_M^ϕ of the flux at N interior grid points as the root-mean-square percentage deviation error:

$$\sigma_{Mi}^\phi = \frac{\phi_i - \widetilde{\phi}_i}{\widetilde{\phi}_i} \times 100\% \,; \qquad \sigma_M^\phi = \sqrt{\frac{1}{N}\sum_i^N \left(\frac{\phi_i - \widetilde{\phi}_i}{\widetilde{\phi}_i}\right)^2} \times 100\% \,. \tag{31}$$

The model error of each P_L solution, for $L = 1, 3, 5, 7$, with respect to S_{24} result for this problem along the line $y = 5$ mm is shown in Fig. 8. The ray effect causes the model error oscillations, which are larger near the source. The total model errors of the flux with respect to S_{24} transport solution are $\sigma_M^\phi(P_1) = 4.32\%$ and $\sigma_M^\phi(P_7) = 1.43\%$, for the P_1 and P_7 approximations respectively. The P_1 model error is higher than the P_7 model error, then the P_7 approximation performs better that the diffusion (P_1) approximation.

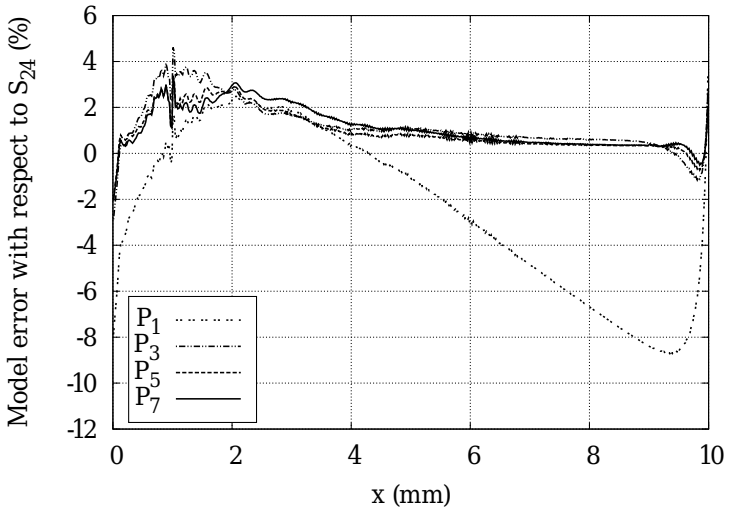

Figure 8: Relative differences of P_L photon fluxes with respect to S_{24} solution through medium center ($y = 5$ mm), for 2D case B.

In Fig. 9 contour maps of photon fluxes calculated with P_1 and P_9 approximations are shown in logarithmic scale. The S_{24} $\log_{10}$ flux distribution is shown in Fig. 10. Although P_1 approximation does not behave so badly in this problem, the results confirm that it is necessary to use high order P_L approximations to obtain accurate solutions.

3.2.3. 2D anisotropic scattering test case C

In this case, we define an anisotropically scattering medium whose optical properties are $\mu_s = 5$ mm^{-1} and $\mu_a = 0.001$ mm^{-1}. The anisotropy factor is $g = 0.8$ and the reduced scattering coefficient is $\mu_s' = (1 - g)\mu_s = 1$ mm^{-1},

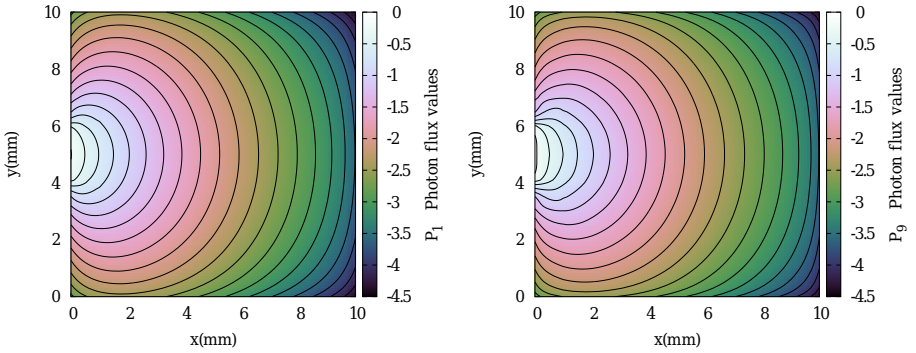

Figure 9: Log_{10} of the photon flux distributions, obtained with P_1 (left), and P_9 (right) approximations, for 2D case B.

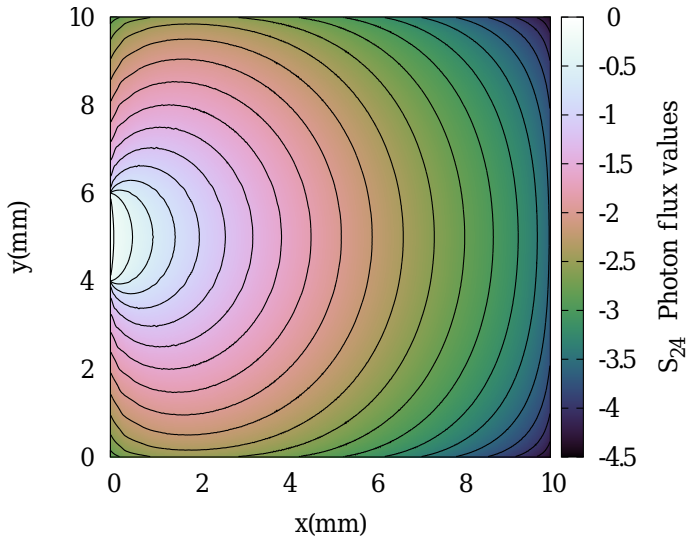

Figure 10: Contour map of the S_{24} ($\log_{10}$) photon flux for 2D case B.

thus we have that $\mu_a \ll \mu_s'$. This problem is also inspired in a case presented in [16]. As $g \leq 0.8$, the scattering cross-section has been modelled according to the Henyey-Greenstein phase function (4).

The results for the photon fluxes are displayed in Figs. 11 and 13. Fig. 11 shows the photon fluxes along X-axis through medium center ($y = 5$ mm), modeled by P_L ($L = 1, 3, 5, 7$) together with the S_{24} solution.

The model error of P_L photon fluxes, for $L = 1, 3, 5, 7$, with respect to the S_{24} transport solution is shown in Fig. 12.

The total model error of the flux with respect to S_{24} transport solution

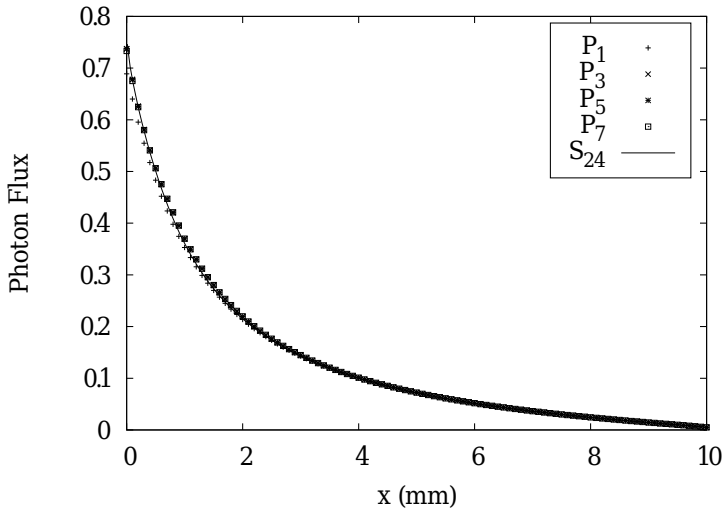

Figure 11: Photon fluxes for the anisotropic scattering case C, along the line $y = 5$ mm.

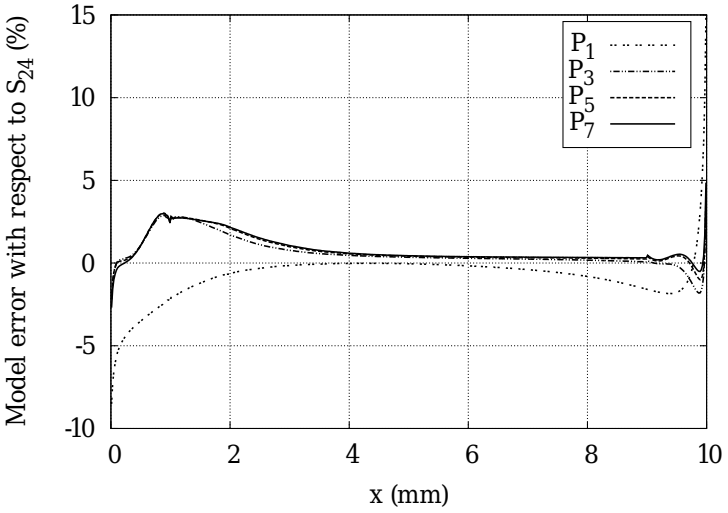

Figure 12: Relative differences of P_L photon fluxes with respect to S_{24} solution through medium center ($y = 5$ mm), for 2D case C.

for the P_1 approximation is $\sigma_M^{\phi}(P_1) = 1.76\%$, and for the P_7 approximation is $\sigma_M^{\phi}(P_7) = 1.20\%$. The model error $\sigma_M^{\phi}(P_1)$ is very low in this simulation, whereas it was higher in the isotropic scattering case of Section 3.2.2. Although

in this case we have considered an anisotropic scattering medium, it is also a more diffusive problem than the isotropic case of Section 3.2.2, because now the ratio between μ_a and μ'_s is lower ($\mu_a/\mu'_s = 0.001$).

Fig. 13 shows the contour maps of log 10 photon fluxes calculated with P_1 (left) and P_9 (right) approximations.

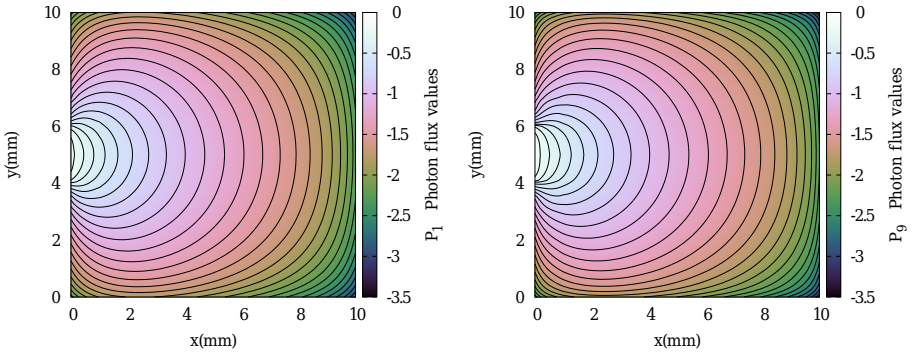

Figure 13: Contoured $\log_{10}$ of the P_1 (left) and P_9 (right) photon flux distributions, for the anisotropic scattering case C.

The results confirm that the P_L approximations are able to reproduce the anisotropic scattering effects on the medium.

3.3. Two-dimensional heterogeneous media

We study the application of the spherical harmonics-nodal collocation method in heterogeneous media whose geometry is a two-dimensional square. The first two cases considered in this Section were presented in [19] and [9], and the geometrical simulations consist of a square with an inner central squared void and a square including a channel at the periphery. The third case is chosen to analyze the effect of anisotropic scattering in heterogeneous media; in this latter case we consider the geometry of the channeling problem. In all the heterogeneous cases the value of photon flux at the external source is taken to be 10^4 photons/mm^2 [35]. The numerical results show the influence of void-like regions on the transport of photons.

3.3.1. Simulation geometry for void-like spaces

A square region with dimensions 120 mm $\times$120 mm enclosing smaller square region of 40 mm $\times$40 mm is considered [19]. The geometry is shown in Fig. 14.

We study the propagation of photons through void-like regions. Human tissue usually consists of several layers having different absorption and scattering properties. In this case, the small square region is assigned low-scattering and absorption coefficients, in order to simulate void-like regions in the human body, such as the scattering and absorption free regions in the brain, which are filled with the cerebrospinal-fluid (CSF).

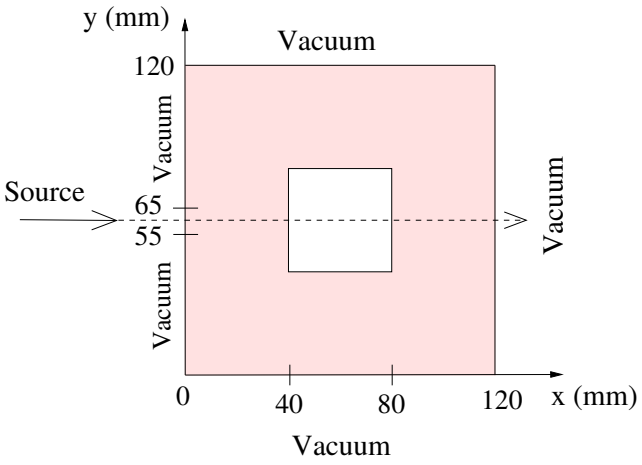

Figure 14: Geometry of two-dimensional void-like spaces.

The scattering and absorption coefficients for the outer square region are $\mu_s = 0.5$ mm^{-1} and $\mu_a = 0.005$ mm^{-1}, and for the inner square $\mu_s = 0.01$ mm^{-1} and $\mu_a = 0.0001$ mm^{-1}, then $\mu_a \ll \mu_s$. An isotropic source with size 10 mm is symmetrically placed at $x = 0$ mm, 55 mm $< y <$ 65 mm, and vacuum boundary conditions are applied on the other boundaries.

We study the accuracy of the P_L SHNC solutions to investigate the flux distribution inside the inner square. For the P_L calculations, a spatial discretization of the medium consisting of 24×24 square nodes with side length 5 mm and an order $M = 4$ of Legendre polynomials has been used in the nodal collocation method. Fig. 15 shows the $\log_{10}$ of the photon flux results along the horizontal line $y = 60$ mm passing through the center of the inner square. The figure shows a comparison between the P_1, P_7 and S_{24} solutions. The S_{24} solution was calculated with a 360×360 mesh grid and a convergence criterion of 10^{-7}.

As can be seen in Fig. 15, P_1 approximation predicts an almost constant photon flux throughout the void, whereas the P_7 and S_{24} calculations show a slight attenuation of the flux inside the void. This confirms the results of Aydin et al. [19]. The total model error of the P_1 flux with respect to S_{24} transport solution is $\sigma_M^{\phi}(P_1) = 4.45\%$. From the figure, we observe no significant differences between the P_7 and S_{24} solutions, being the total model error of the P_7 flux $\sigma_M^{\phi}(P_7) = 0.56\%$, that confirms the capability of the high order P_L approximation to deal with this type of problems.

In Fig. 16 contour plots of the log 10 photon fluxes are shown for the void-like region (40 mm $< x <$ 80 mm). The differences observed between P_1 and P_7 contour maps match those of Fig. 15.

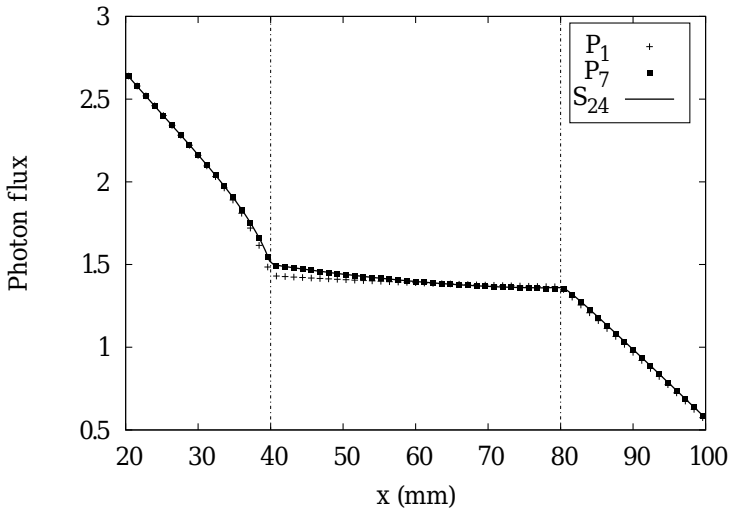

Figure 15: Log_{10} of the photon flux calculated with P_1, P_7 and S_{24}, inside a low density square region.

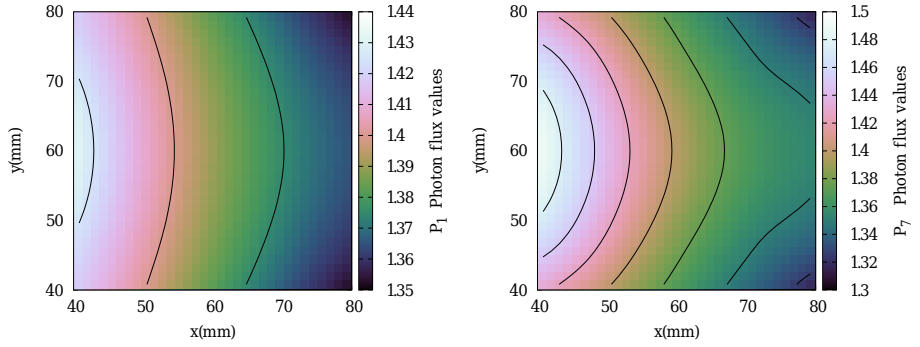

Figure 16: Contoured $\log_{10}$ of the photon flux values, obtained with P_1 (left), and P_7 (right) approximations, for the void-like region.

3.3.2. Simulation geometry for channeling problem

The brain is embedded in such an almost absorption and scattering-free fluid, this layer of CSF forms a boundary between the outside tissues and the brain [9, 19]. The geometry of this problem that simulates approximately this situation is shown in Fig. 17. A 100 mm $\times$100 mm square region with $\mu_s = 0.5$ mm^{-1} and $\mu_a = 0.005$ mm^{-1} is considered ($\mu_a \ll \mu_s$). The void-like region (CSF fluid) is represented by a structure of size 4 mm thick with $\mu_s = 0.01$ mm^{-1} and $\mu_a = 0.0001$ mm^{-1}, which surrounds a 76 mm $\times$76 mm inner square. An isotropic source with size 4 mm is centered at $x = 0$ mm, 48 mm $< y <$ 52

mm, and vacuum boundary conditions are applied on all the other boundaries.

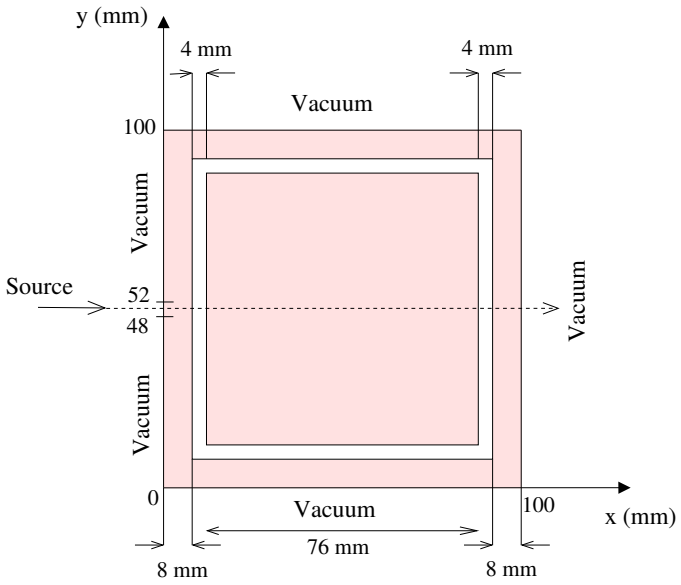

Figure 17: Geometry of two-dimensional channeling problem.

The P_1, P_7 and S_{24} photon flux results are displayed in Fig. 18, in logarithmic scale, along the line $y = 50$ mm passing through the medium center. We consider a spatial mesh of 25×25 square nodes with side length 4 mm in the P_L calculations with an order $M = 4$ of Legendre polynomials, and a 1250×1250 mesh grid for the S_{24} calculation, with a convergence criterion of 10^{-7}.

Fig. 18 shows good agreement between the P_7 and S_{24} solutions, being the total model error of the P_7 flux with respect to the S_{24} solution $\sigma_M^{\phi}(P_7) = 5.97\%$. On the other hand, the P_1 approximation shows significant discrepancies. Through the first (8 mm $< x <$ 12 mm) and the second (88 mm $< x <$ 92 mm) void-like channels, P_1 and P_7 approximations predict an almost constant photon intensity, but inside the first channel the P_1 approximation underestimates the flux, and through the second channel P_1 flux values are higher than the ones predicted by P_7 approximation. We also observe that after the first void-like channel, the P_7 flux values show faster decay ($x > 12$ mm). Unlike the P_1 results, the P_7 flux continues decreasing even behind the second channel.

In Fig. 19 contour plots of photon fluxes obtained with P_1 (left) and P_7 (right) approximations are displayed. The differences observed between P_1 and P_7 predictions in this figure just reflect the effects of the channel seen in Fig. 18. Our results also confirm the necessity of using high order L, in order to obtain accurate P_L solutions of the photon fluxes especially in void-like regions.

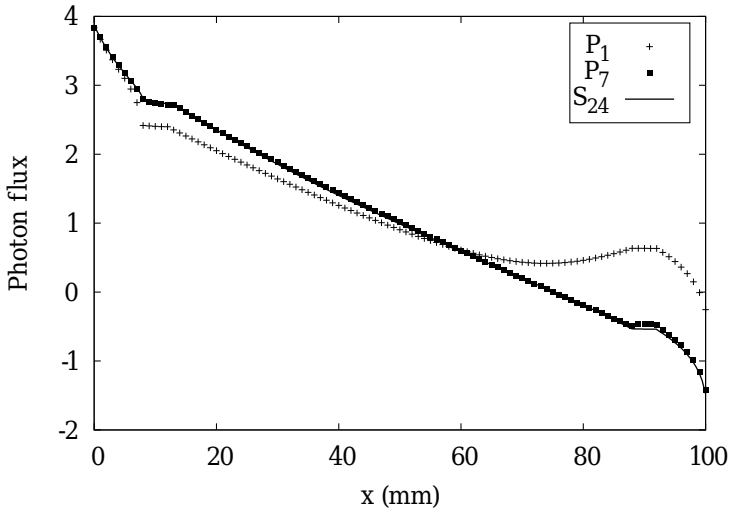

Figure 18: Log_{10} of the photon fluxes for the 2D CSF-layered problem.

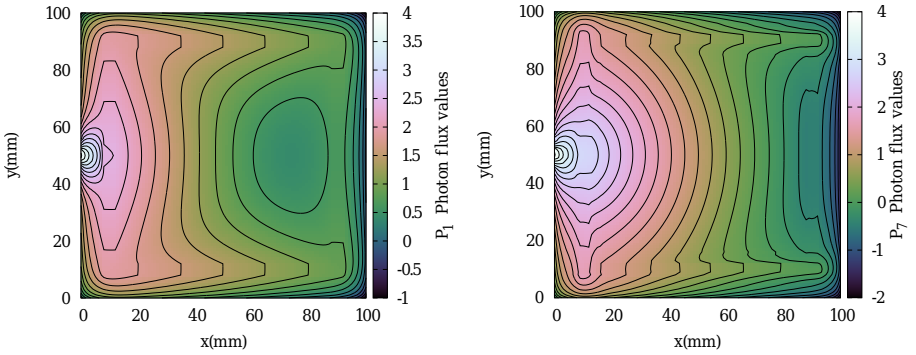

Figure 19: Contoured $\log_{10}$ of the photon flux values, obtained with P_1 (left), and P_7 (right) approximations, for the CSF-layered problem.

3.3.3. Influence of anisotropic scattering in heterogeneous media

As a final example we consider again the CSF-layered problem whose geometry is shown in Fig. 17. We investigate the effect of the anisotropy factor g in modeling the propagation of photons through the same heterogeneous channeling problem. We take the same scattering and absorption optical properties as in Section 3.3.2 but, in this case, the anisotropy factor g is taken to be 0.92 in the region outside the void-like channel and in the 76 mm $\times$76 mm inner square, so the reduced scattering coefficient is $\mu_s' = (1-g)\mu_s = 0.04$ mm^{-1}, and $\mu_a/\mu_s' = 0.0125$ in this region.

Fig. 20(a) shows $\log_{10}$ photon fluxes from P_L ($L = 1, 3, 5, 7$) approximations along the line $y = 50$ mm. For the media having anisotropy factor of $g = 0.92$, we modeled the anisotropic scattering using the Henyey-Greenstein (H-G) phase function (4) with 7 Legendre expansion coefficients. We consider a spatial mesh of 25×25 nodes with side length 4 mm.

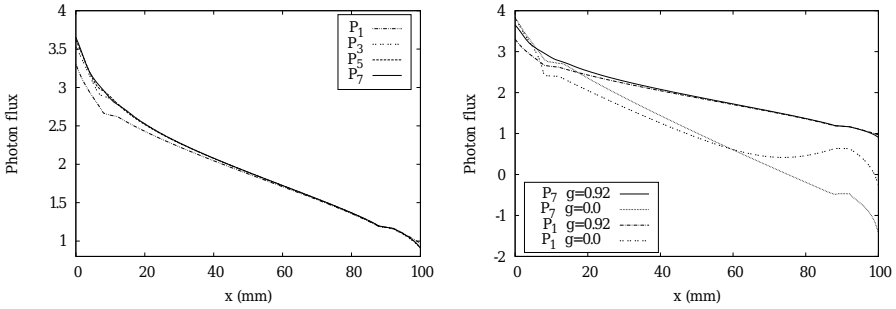

(a) (b)

Figure 20: Influence of anisotropic scattering in heterogeneous media. In (a), $P_1 - P_7$ photon fluxes. In (b), $g = 0$ and $g = 0.92$ P_1 and P_7 calculations for the same CSF-layered problem.

In Fig. 20(b) we compare the P_1 and P_7 solutions of the RTE for the case with anisotropic scattering to the corresponding solutions taking $g = 0$ in both regions. Then, in this latter case we have that $\mu_s' = \mu_s = 0.5$ mm^{-1} and $\mu_a/\mu_s' = 0.01$ in the region outside the channel. We observe significant differences between isotropic and anisotropic scattering cases, and P_1 and P_7 differences are more remarkable when isotropic scattering ($g = 0$) in all the media is considered. Fig. 21 displays the contoured map of the P_7 ($\log_{10}$) photon flux, for the same anisotropic scattering problem.

Next we present calculations for this case using the simplified approximate Mie (SAM) phase function (5) to model the anisotropic scattering. The P_1 and P_7 $\log_{10}$ photon flux distributions calculated using the two phase functions, H-G and SAM, are compared in Fig. 22 along the horizontal line $y = 50$ mm, for the left half of the medium (0 mm $< x <$ 50 mm). The location of the first channel is marked in the figure.

For the P_7 approximation, we used H-G function with 7 Legendre expansion coefficients whereas only 3 Legendre coefficients were taken when the SAM function was employed. Due to the high value of the anisotropy factor ($g > 0.8$), a high number of Legendre coefficients was required for the H-G function to accurately compute the P_7 approximation. On the contrary, we numerically observe that, when dealing with SAM function, only the first 3 coefficients are required to match the accuracy of the H-G P_7 approximation.

From Fig. 22 we observe that the influence of the anisotropy is more important with high order P_L approximation, and the largest discrepancies between H-G and SAM functions occur for P_7 approximation around the void-like chan-

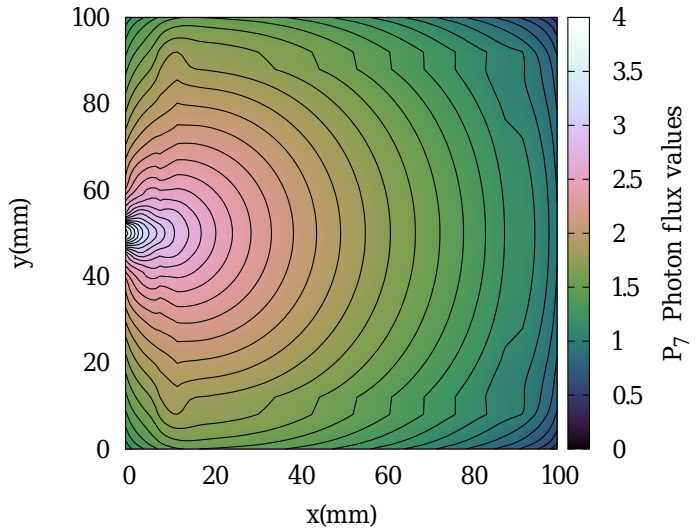

Figure 21: Contoured $\log_{10}$ of the P_7 photon flux, for the anisotropic CSF-layered problem.

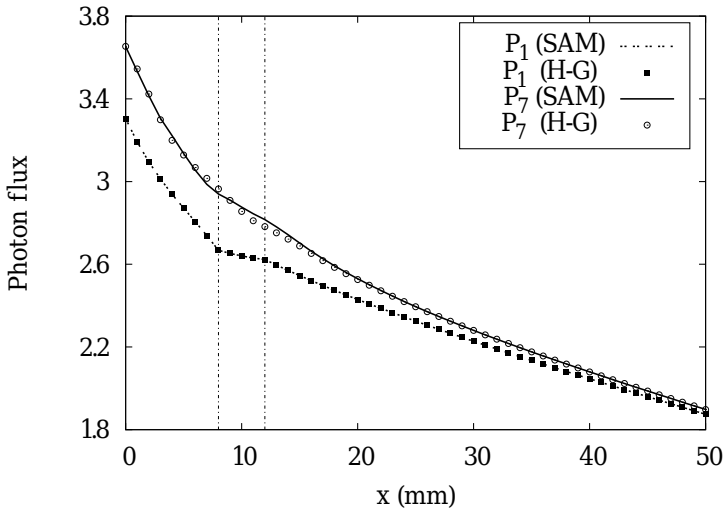

Figure 22: A comparison between the results obtained with H-G and SAM phase functions.

nel.

4. Conclusions

We have reviewed the multi-dimensional spherical harmonics P_L equations when applied to optical tomography. The P_L equations, for arbitrary angular order L, have been formulated as a vector-valued diffusive second order differential equation. Surface source and vacuum boundary conditions have been approximated using Marshak's conditions and computed for arbitrary order L.

We have applied a nodal collocation method for the spatial discretization of the P_L equations, based on the expansion of the angular neutronic moments in terms of orthonormal Legendre polynomials. The main advantage of the method is the lower dimension and good characteristics of the matrix associated to the algebraic problem. The method is able to work with nodes of big size using a moderate number of Legendre polynomials giving satisfactory results. The computation using big size nodes reduces the dimension of the algebraic problem in comparison to other methods like finite elements or finite differences.

As a first test of the method, we have examined the transport of photons through 1D homogeneous media, comparing the results against the exact analytical solution and also with the results provided by ONEDANT (S_N) code, showing that P_1 approximation fails to describe the light propagation correctly, whereas higher order P_L approximations (P_7, P_9) show accurate results in comparison to the exact solution.

We have also tested several 2D homogeneous isotropic and anisotropic cases. Again, the P_L computations are compared with the transport approximation obtained from the S_N code TWODANT. The results confirm that the P_L approximation is able to reproduce the isotropic and anisotropic scattering effects on the medium without suffering from ray effect as S_N approximation does. Finally, we have studied 2D heterogeneous media with void-like regions such as low-scattering and absorption channels. In both types of media, an isotropic scattering model is studied, and in the latter case, which corresponds to the channeling problem, we consider also the anisotropic model, comparing results from the Henyey-Greenstein (H-G) and simplified approximated Mie (SAM) phase functions. The largest discrepancies between H-G and SAM phase functions occur for P_7 approximation around the void-like channel. We remark the necessity of using P_L approximations for $L > 1$, even in cases where the diffusion approximation does not fail completely. Due to the ill-posed nature of these type of problems, even small errors in modeling can cause large errors in the reconstructions. Therefore, it is important to have a computationally feasible model that describes light propagation in the medium accurately.

In summary, in this work we have shown that the diffusive P_L spherical harmonics equations have several advantages if they are compared with S_N or SP_L equations and that this model can be efficiently applied to optical tomography obtaining good results.

Acknowledgments

This work has been partially supported by the Spanish Ministerio de Economía y Competitividad under project ENE-2014-59442-P and by the Generalitat Valenciana under project PROMETEO II/2014/008.

References

[1] Haisch C. Optical Tomography. Annu Rev Anal Chem 2012;5:55–77.

[2] Qi J, Ye Z. Computed Tomography Laser Mammography Optical as an adjunct to mammography in the diagnosis of patients with dense breast. Clin Imag 2013;37(2):289–294.

[3] Klose AD, Netz U, Beuthan J, Hielscher AH. Optical tomography using the time-independent equation of radiative transfer Part 1: forward model. J Quant Spectrosc Radiat Transf 2002;72(5):691–713.

[4] Dudko OK, Weiss GH. Photon Diffusion in Biological Tissues. Diffusion Fundamentals 2005;2:114.1–114.21.

[5] Venugopal V, Intes X. Recent advances in optical mammography. Curr Med Imaging Rev 2012;8(3):244–259.

[6] Aydin ED, De Oliveira CRE, Goddard AJH. A finite element-spherical harmonics radiation transport model for photon migration in turbid media. J Quant Spectrosc Radiat Transf 2004;84:247–260.

[7] Boas DA. Diffuse photon probes of structural and dynamical properties of turbid media: Theory and biomedical applications. PhD Thesis, University of Pennsylvania, USA, 1996.

[8] Gibson AP, Hebden JC, Arridge SR. Recent advances in diffuse optical imaging. Phys Med Biol 2005;50(4):R1–R43.

[9] Hielscher AH, Alcouffe RE, Barbour RL. Comparison of finite-difference transport and diffusion calculations for photon migration in homogeneous and heterogeneous tissues. Phys Med Biol 1998;43:1285–1302.

[10] Arridge SR, Dehghani H, Schweiger M, Okada E. The finite element model for the propagation of light in scattering media: a direct method for domains with nonscattering regions. Med Phys 2000;27:252–64.

[11] Firbank M, Arridge SR, Schweiger M, Delpy DT. An investigation of light transport through scattering bodies with non-scattering regions. Phys Med Biol 1996;41:767–83.

[12] Arridge SR. Optical tomography in medical imaging. Inverse Problems 1999;15:R41–R93.

[13] Tahir KB, De Oliveira CRE, Katsimichas S, Dainty JC. A comparison between finite element transport and Monte Carlo solutions for photon propagation. Proc Appl Opt Opto-electronics 1996: 58–63.

[14] Kaltenbach JM, Kaschke M. Frequency- and time-domain modelling of light transport in random media. Proc. SPIE ISll, 1993. p. 65–86.

[15] Josef JA, Morel JE. Simplified spherical harmonic method for coupled electronphoton transport calculations. Phys Rev E 1998;57(5):6161–6171.

[16] Klose AD, Larsen EW. Light transport in biological tissue based on the simplified spherical harmonics equations. J Comp Phys 2006;220:441–470.

[17] Brunner TA, Holloway JP. Two dimensional time dependent Riemann solvers for neutron transport. J Comput Phys 2005;210(1):386–399.

[18] McClarren RG, Hollway JP, Brunner TA. Analytic P_1 solutions for time-dependent, thermal radiative transfer in several geometries. J Quant Spectrosc Radiat Transf 2008;109:389–403.

[19] Aydin ED, De Oliveira CRE, Goddard AJH. A comparison between transport and diffusion calculations using a finite element-spherical harmonics radiation transport method. Med Phys 2002;29(9):2013–2023.

[20] Duderstadt JJ, Hamilton LJ. Nuclear Reactor Analysis. New York: Wiley, 1976.

[21] Courant R, Hilbert D. Methods of Mathematical Physics, Vol. I. Wiley-Interscience, 1962.

[22] Stratton A. Electromagnetic Theory. New York: McGraw-Hill, 1941.

[23] Van de Hulst HC. Multiple Light Scattering: Tables, Formulas and Applications. New York: Academic, 1980.

[24] Liu P. A new phase function approximating to Mie scattering for radiative transport equations. Phys Med Biol 1994;39:1025–1036.

[25] Stacey WM. Nuclear Reactor Physics. New York: Wiley, 2001.

[26] Hébert A. Development of the nodal collocation method for solving the neutron diffusion equation. Ann Nucl Energ 1987;14(10):527–541.

[27] Verdú G, Ginestar D, Vidal V, Muñoz-Cobo JL. λ modes of the neutron diffusion equation. Ann Nucl Energ 1994;21(7):405–421.

[28] Capilla M, Talavera CF, Ginestar D, Verdú G. A nodal collocation method for the calculation of the lambda modes of the P_L equations. Ann Nucl Energ 2005;32:1825–1853.

[29] Capilla M, Talavera CF, Ginestar D, Verdú G. Application of a nodal collocation approximation for the multidimensional P_L equations to the 3D Takeda benchmark problems. Ann Nucl Energ 2012;40:1–13.

[30] Saad Y. SPARSKIT: a basic tool kit for sparse matrix computations-Version 2. http://www-users.cs.umn.edu/~saad/software/SPARSKIT, 1994.

[31] Capilla M, Talavera CF, Ginestar D, Verdú G. Nodal collocation method for the multidimensional P_L equations applied to neutron transport source problems. Ann Nucl Energ 2016;87:89–100.

[32] Alcouffe RE, Baker RS, Brinkley FW, Marr DR, O'Dell RD, Walters WF. DANTSYS: A diffusion accelerated neutral particle transport code system. Los Alamos National Laboratory, LA-12969-M, 1995.

[33] Piessens R, Doncker-Kapenga E, Überhuber CW, Kahaner D. QUADPACK: A subroutine package for automatic integration. Springer-Verlag, ISBN 978-3-540-12553-2, 1983.

[34] O'Dell RD, Alcouffe RE. Transport calculations for nuclear analyses: theory and guidelines for effective use of transport codes. ANL Manuscript LA-10983-MS, 1987.

[35] Aydin ED. Three-dimensional photon migration through voidlike regions and channels. Appl Opt 2007;46(34):8272–8277.

[36] Mohan PS, Tarvainen T, Schweiger M, Pulkkinen A, Arridge SR. Variable order spherical harmonic expansion scheme for the radiative transport equation using finite elements. J Comp Phys 2011;230:7364–7383.